ACS APPLIED MATERIALS & INTERFACES

Research Article

www.acsami.org

Ordered Mesoporous Carbon Electrodes for Li–O_2 Batteries

Jin-Bum Park,[†] Jinwoo Lee,[‡] Chong Seung Yoon,[§] and Yang-Kook Sun*[,†,⊥]

[†]Department of Energy Engineering and [§]Department of Materials Science and Engineering, Hanyang University, Seoul 133-791, Republic of Korea

[‡]Department of Chemical Engineering, Pohang University of Science and Technology (POSTECH), Pohang, Kyungbuk 790-784, Republic of Korea

[⊥]Chemistry Department, Faculty of Science, King Abdulaziz University, Jeddah, Saudi Arabia

ABSTRACT: Ordered mesoporous carbon (OMC) with highly ordered pore channels was applied as an oxygen-side electrode for a Li–O_2 battery. To evaluate the effect of the pore channel size on battery performance, we employed OMCs possessing two different pore sizes (6 and 17 nm). When cycled at a current density of 200 mA g^{-1}_{carbon}, the OMC electrodes reduced polarization in the oxygen evolution reaction by 0.1 V compared to those consisting of conventional super P carbon electrode. X-ray diffraction and transmission electron microscopy of the discharged oxygen electrodes provided evidence for the formation of amorphous Li_2O_2, a product of the oxygen reduction reaction, inside the OMC pores rather than on the electrode surface as in the case of the super P electrode. The OMC electrodes were also effective at high current densities (500 mA g^{-1}_{carbon} and 1000 mA g^{-1}_{carbon}).

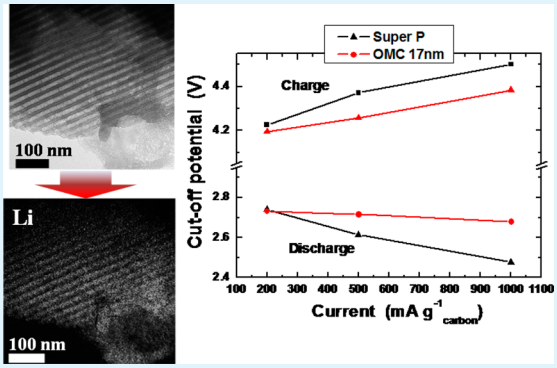

KEYWORDS: *Li–O_2 batteries, ordered mesoporous carbon, Li_2O_2, air electrode*

INTRODUCTION

To meet the ever-increasing global energy demand, new energy storage devices need to provide higher energy density than traditional Li-ion batteries can. Among the rechargeable battery devices investigated to date, nonaqueous Li–O_2 cells remain the most attractive alternative system largely because of their high energy density.[1−3] However, several lingering issues about the Li–O_2 cell still impede its practical application.[4−6] Among the many problems, to decrease the charging potential, namely oxygen evolution reaction (OER) potential, researchers have employed porous carbon,[7,8] metal (oxide) catalyst,[9−13] and their composites[14−16] as oxygen electrode materials. Because carbon materials have high surface area and large pore volume for Li_2O_2 deposition, they are used for cathode materials of Li–O_2 cells. To increase the capacity and decrease the OER potential simultaneously, researchers have used several metal (oxide) catalysts and carbon composite material for the cathode of Li–O_2 cells. By using a catalyst, it was possible to lower the charging potential under 4 V corresponding overpotential of 1.1 V.[14,16] There has also been many attempts to decrease the charging potential of Li–O_2 cells by changing the morphology of the carbon materials without catalyst.[17,18] But it is hard to decrease the OER potential because of the low electronic conductivity of Li_2O_2. In addition, there have been a few approaches that solve the low rate capability.[18,19]

Among the various carbon materials, ordered mesoporous carbon(OMC) with pore sizes ranging from 2 to 50 nm can be a potential candidate electrode material because of the high surface area, various pore sizes, and structures.[20,21] Other authors[22,23] have already applied the mesoporous carbon as an oxygen electrode for Li–O_2 cells, but it was difficult to directly observe the lithium peroxide by transmission electron microscopy (TEM) after discharge because of the various pore sizes and disordered pore distributions of mesoporous carbon. Recently, Guo et al.[18] employed the ordered mesoporous carbon as catalyst of Li–O_2 cells and reported that the ordered mesoporous channels and hierarchical mesoporous/macroporous structure of OMC facilitated the electrolyte immersion and Li^+ diffusion and provided an effective space for O_2 diffusion and O_2/Li_2O_2 conversion. In this work, we used two different highly ordered mesoporous carbons with a pore size of 6 nm (OMC-6) and 17 nm (OMC-17) for an oxygen electrode without catalyst. By using the OMC material as an oxygen electrode, it was demonstrated that the charge potential can be lowered while improving the rate capability compared with super P carbon. The morphology of the discharge product that formed on the OMC material was found to be different from that of super P.

EXPERIMENTAL SECTION

Synthesis of OMC-6. OMC-6 was prepared following the reported procedure.[24] Initially, 2.6 g of Pluronic F-127 was dissolved in 13.0 g of ethanol with 1.63 g of 0.2 M HCl and stirred for 1 h at 40 °C. Then,

Received: October 3, 2013
Accepted: November 15, 2013
Published: November 15, 2013

3.4 g of TEOS and 8.1 g of resols' ethanolic solution (20 wt % in ethanol) were added. After stirring for 2 h, the solution was poured into a Petri dish for ethanol evaporation. After 8 h, the composite film was thermopolymerized at 100 °C in an oven for 1 day. The as-synthesized film was carbonized in a N_2 atmosphere at 350 °C for 3 h and 900 °C for 2 h in a tube furnace (heating rate, 1 °C min^{-1}). Finally, the product (C-SiO_2 nanocomposite) was treated with 10 wt % HF solution to dissolve the silica.

Synthesis of OMC-17. The ordered mesoporous carbon with 17 nm pores was synthesized using poly(ethylene oxide)-b-polystyrene block copolymer (PEO-b-PS) as a structure-directing agent.[25,26] The Mn value of PEO-b-PS was 30,200 g mol^{-1} (16.5 wt % PEO) and its polydispersity index was 1.34. In a typical synthesis, 0.4 g of PEO-b-PS was dissolved in 10 mL of tetrahydrofuran (THF). Then, 0.19 g of 0.2 M HCl was added. After 10 min, 0.78 g of TEOS and 3.87 g of resols' ethanolic solution were added and the solution was stirred for 1 h. The solution was poured into a Petri dish for THF evaporation. After 8 h, the composite film was thermopolymerized at 100 °C in an oven for 1 day. The as-synthesized film was carbonized in N_2 atmosphere at 450 °C for 3 h and 900 °C for 2 h in a tube furnace (heating rate, 1 °C min^{-1}). Finally, the C-SiO_2 nanocomposite was treated with a 10 wt % HF solution.

Electrode Preparation and Measurement. The sample of carbon materials and polyvinylidene fluoride binder (PVDF) with a mass ratio of 8:2 was mixed in a N-methyl-2-pyrrolidone (NMP) solution, and then the resulting slurry was coated on the current collector of the gas diffusion layer(GDL, TGP-H-030 carbon paper, Torray). The coated electrode was dried at 100 °C under vacuum for 12 h to remove the residual solvent. The mass loading of carbon materials on the GDL (carbon-electrode) was about 1 mg_{carbon} cm^{-2}. The R2032 coin-type cell was assembled in an argon-filled glovebox with a water and oxygen content, both less than 0.1 ppm. The cell consisted of a metallic lithium foil anode (thickness, 400 mm) and the aforementioned carbon electrode. A glass filter (Whatman) separated the anode from the cathode, and a solution of 1 M $LiCF_3SO_3$/tetra ethylene glycol dimethyl ether (TEGDME) was used as the electrolyte. The cell was electrochemically investigated using galvanostatic cycling with a VMP3 Biologic Instrument. The charge−discharge test was carried out in time-controlled mode at a current density of 200 mA g^{-1}_{carbon} for 10 h, and the cells were placed in an oxygen-filled chamber with a pressure slightly higher than 1 atm.

Characterization. Field-emission SEM (FE-SEM, S-4800, Hitachi) and high-resolution TEM (HR-TEM, model JEM-2010, JEOL) were used to observe the morphology and structure of mesoporous carbon materials and carbon electrode after discharge. The discharged electrode was protected from exposure to air during transfer to the SEM chamber by conductive tape applied in the glovebox. X-ray diffraction was carried out using a Rigaku instrument with a Cu-Ka radiation source. For this test, the discharged electrodes were washed with TEGDME and dried under vacuum to remove the residual solvent. The surface area and porosity of mesoporous carbon were determined by using a Quantachrome Autosorb-iQ-MP automated gas adsorption system using nitrogen as the adsorbate at a temperature of 77 K. The specific surface area was calculated using the Brunauer−Emmett−Teller (BET) method, and the pore diameters were obtained from the adsorption branch of the isotherm using the Barrett−Joyner−Halenda (BJH) method. Small-angle X-ray scattering (SAXS) experiments were carried out on the 4C1 SAXS station at the Pohang Accelerator Laboratory using X-rays (7.8 keV, 0.16 nm)

RESULTS AND DISCUSSION

Figures 1a-d show the SEM and TEM images of OMC-6 and OMC-17. It can be seen that the openings of the pores were uniformly distributed on the surface of OMC-6 and OMC-17. Images b and d in Figure 1 show the TEM images of OMC, which has many striped lines arising from the pore structure. The TEM images clearly demonstrated that OMC-6 and OMC-17 have a highly ordered two-dimensional structure

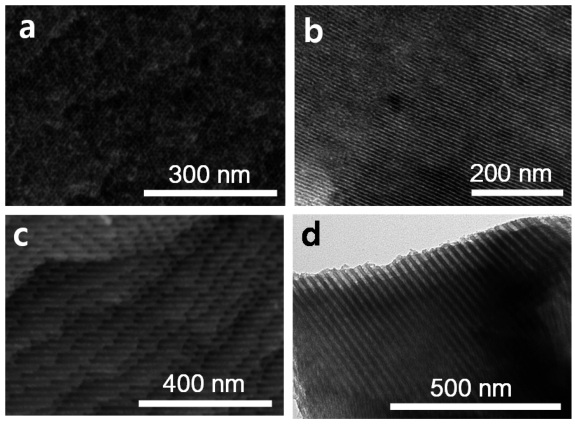

Figure 1. Scanning electron microscopy (SEM) and transmission electron microscopy (TEM) images of (a, b) OMC-6 and (c, d) OMC-17.

created by the pore-making reagents. Figure 1 also confirmed that OMC-17 has a larger pore diameter than OMC-6.

The porosity of the OMC was investigated by nitrogen sorption analysis, which is displayed in Figure 2a. The Brunauer−Emmett−Teller (BET) surface areas of OMC-6 and OMC-17 were as high as 1645 and 1311 m^2 g^{-1}, respectively, with a large pore volume of 1.68 and 1.55 cm^3 g^{-1}. The OMC-6 exhibited a quite uniform pore size distribution, whereas OMC-17 had a wider pore size distribution in which the pore diameter ranged from 16 to 20 nm. Representative SAXS patterns of OMC-6 and OMC-17 are shown in Figure 2b. The corresponding $d_{spacing}$ values of the OMCs were 9.4 and 24.2 nm, respectively. The main peaks, marked by the arrows, were observed and suggested a short-range ordered hexagonal structure.[27] The peaks had a tendency to be shifted to larger q values with a larger pore size. The OMC materials show typical patterns of an ordered cylindrical mesostructure with relative scattering vector positions $\sqrt{3}$, $\sqrt{4}$, $\sqrt{7}$, and $\sqrt{11}$ of the first-order maximum.[28] The SAXS result and TEM images verify that the OMC materials have a uniform pore size and highly ordered mesoporous structure.

The first discharge−charge profiles of the Li−O_2 cells with three different oxygen cathodes (super P, OMC-6, and OMC-17) are displayed in Figure 3a. In this paper, we selected TEGDME as the solvent, which is more stable than organic carbonate or DME and can also be easily handled.[29,30] As shown in Figure 3a at first discharge, at the current density of 200 mA g^{-1}_{carbon}, the discharge profile of the ORR process is almost identical for all three electrodes. However, in the OER charge process, there was substantial difference among the charge curves of super P and the OMCs. It can be seen from the first cycle profile in Figure 3a that there were two plateaus near 3.5 and 4 V in all three Li−O_2 cells. In the case of OMCs, the charge capacity at 3.5 V reached 1000 mAh g^{-1}_{carbon}, which is twice the capacity of super P during the first cycle. The charge cutoff voltage of the Li−O_2 cells using OMC-6 and OMC-17 was of 4.1 V which is lower than the 4.2 V of the super P. As a result, the energy efficiency of OMC-6 and OMC-17 were 74.7% and 73.8% which were about 3% higher than that of super P (71%). The energy efficiency of the Li−O_2 cell using the smaller pore diameter of OMC-6 was higher than that using OMC-17. The voltage profile of the charge−discharge test by cycling performed on Li−O_2 cells using the OMC-6 and OMC-17 are shown in panels b and c in Figure 3. The OMCs

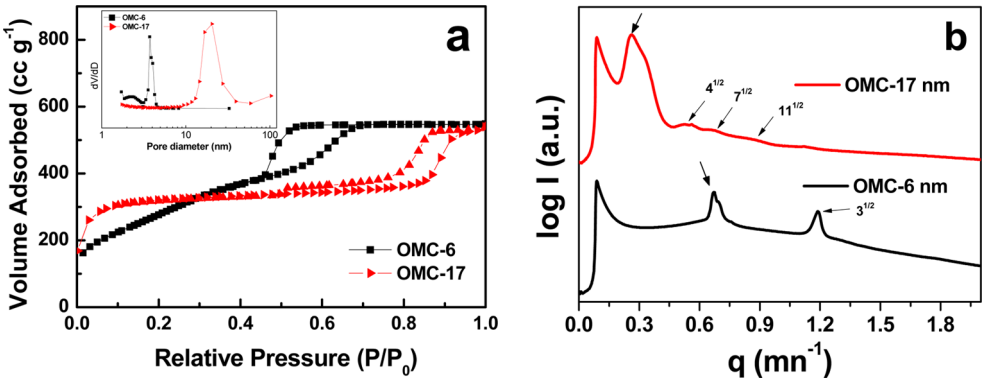

Figure 2. (a) Nitrogen adsorption−desorption and (inset) pore size distribution of OMC-6 and OMC-17, (b) small-angle X-ray scattering (SAXS) patterns of OMC-6 and OMC-17.

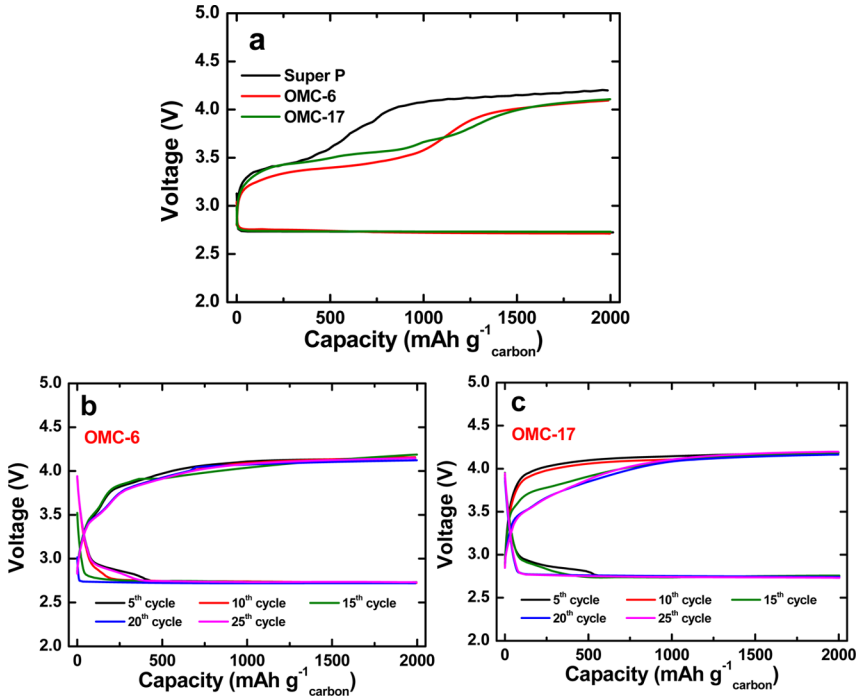

Figure 3. Electrochemical performance testing performed on Li−O_2 cells using a super P electrode, OMC-6 electrode and OMC-17 electrode (a) at the first cycle and cycling behavior of Li−O_2 cells using (b) OMC-6 and (c) OMC-17. Capacity was limited to 2000 mAh g^{-1}_{carbon}. Current: 200 mA g^{-1}_{carbon}.

showed good cycling performances and the discharge−charge voltages changed slightly within a very limited range during the initial 25 cycles (Figure 3b, c).

To identify the discharge product, i.e., the Li_2O_2 and its morphology, the electrodes of OMCs after discharge were characterized by X-ray diffraction (XRD). The XRD patterns in Figure 4a show a noticeable difference in the crystallinity of Li_2O_2 from the discharged electrodes. Among the three samples, the product formed on the super P contained crystallized Li_2O_2 (JCPDS# 73−1640) in the discharge process. However, the Li_2O_2 found on the OMC electrodes was likely amorphous as suggested by the absence of the Li_2O_2 peaks in Figure 4a. Additionally, the selected area electron diffraction (SAED) patterns (Figure 4b, c) of the OMC electrodes confirmed that the Li_2O_2 found on the OMC electrodes was amorphous. It is not clear why the Li_2O_2 formed on the OMC electrodes should be amorphous while those found on the super P electrode should be crystalline based on the XRD and SAED patterns, but the carbon structure of the electrode had a definite effect in determining the structure of Li_2O_2 formed in the discharge process.

In our previous report,[31] the Li_2O_2 product in the discharge process using a super P electrode was composed of a mixture of large, solid or hollow, spherical particles whose diameter was over 1 μm. It was also shown that both amorphous and crystalline forms of Li_2O_2 were observed on the surface of super P. In the OMC case, it was difficult to directly observe the Li_2O_2 particles from the discharged OMC electrodes, which suggests that Li_2O_2 had predominantly nucleated inside the pore channels. Figure 5a confirms that the discharged OMC-17 retains its ordered porous structure. A corresponding elemental mapping of Li obtained using energy-filtered TEM (EFTEM) shown in Figure 5b indicates that the pore channels were enriched in Li, confirming that Li_2O_2 formed along the pore channels. In the case of OMC-6, the ordered structures remained intact during the discharge (Figure 5c), whereas a

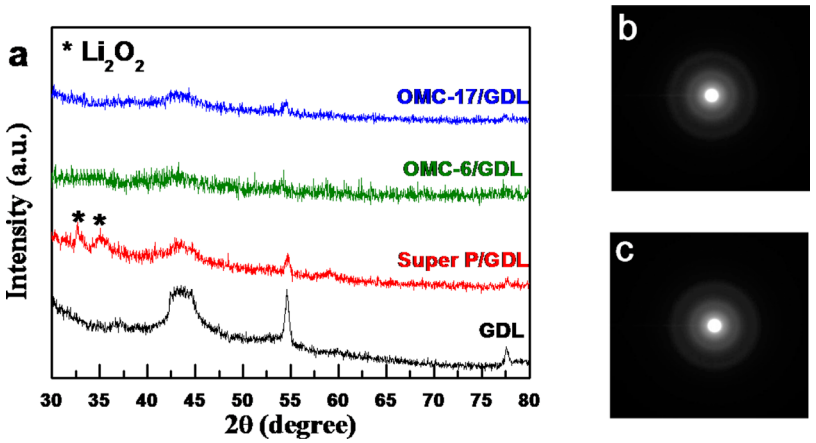

Figure 4. (a) X-ray diffraction pattern of a discharged electrode using a super P electrode, OMC-6 electrode, and OMC-17 electrode. Selected area electron diffraction (SAED) patterns of a discharged electrode of (b) OMC-6 and (c) OMC-17. Discharge capacity was limited to 2000 mAh g^{-1}_{carbon}.

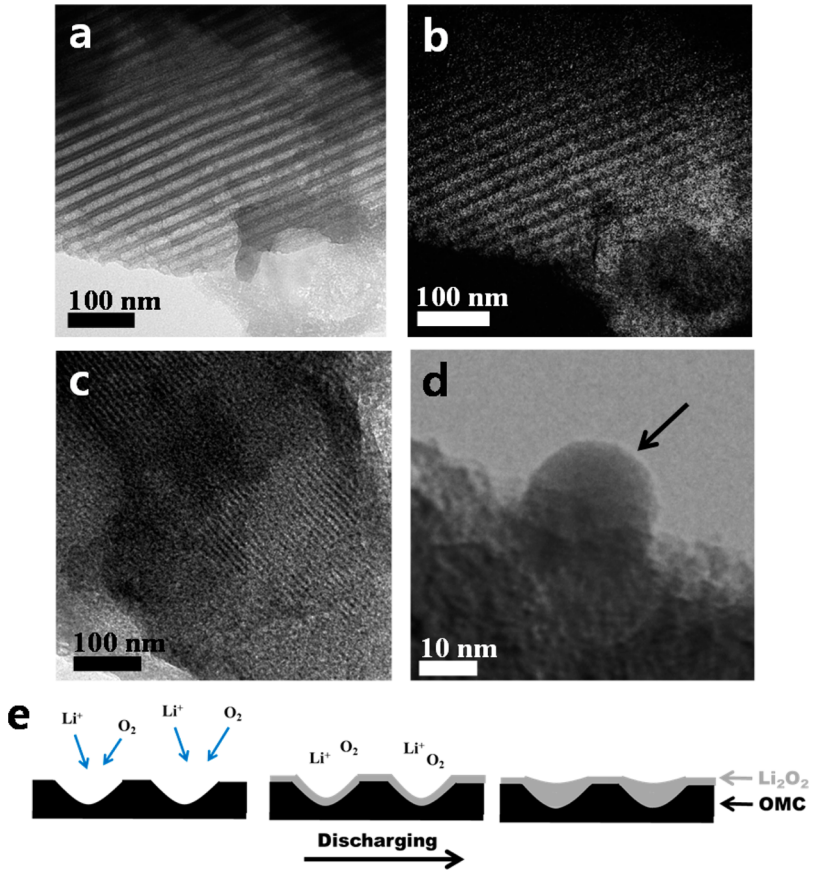

Figure 5. Transmission electron microscopy (TEM) and energy-filtered TEM (EF-TEM) images of discharged electrode using the (a, b) OMC-17 electrode and (c, b) OMC-6 electrode. Discharge capacity was limited to 2000 mAh g^{-1}_{carbon}. (e) The proposed ORR mechanism on the OMC surface.

Li_2O_2 nanoparticle that is 20 nm in diameter was found on the surface of the OMC-6 electrode (indicated by the arrow in Figure 5d). The TEM image in Figure 5d evinces that the Li_2O_2 nucleated on the OMC is amorphous (also confirmed by electron diffraction) and extremely small compared to those formed on the super P electrode. Figure 5e schematically illustrates the possible formation mechanism of Li_2O_2 on the OMC electrodes in the discharge process. At first, nucleated Li_2O_2 nanoparticles are deposited on the surface of OMC.[32] Then, the electronic conductivity dominates the oxygen reduction reaction due to the low electronic conductivity of Li_2O_2. The reaction involving oxygen and the electron will be more likely to occur inside the pores of OMC than outside the pores because of the large exposed surface area inside the pores. Nazar et al.[32] reported that the large Li_2O_2 particles with toroidal structure have high crystallinity by aggregation of Li_2O_2 crystallites at low current density, whereas the small Li_2O_2 particles have low crystallinity at high current density. In our

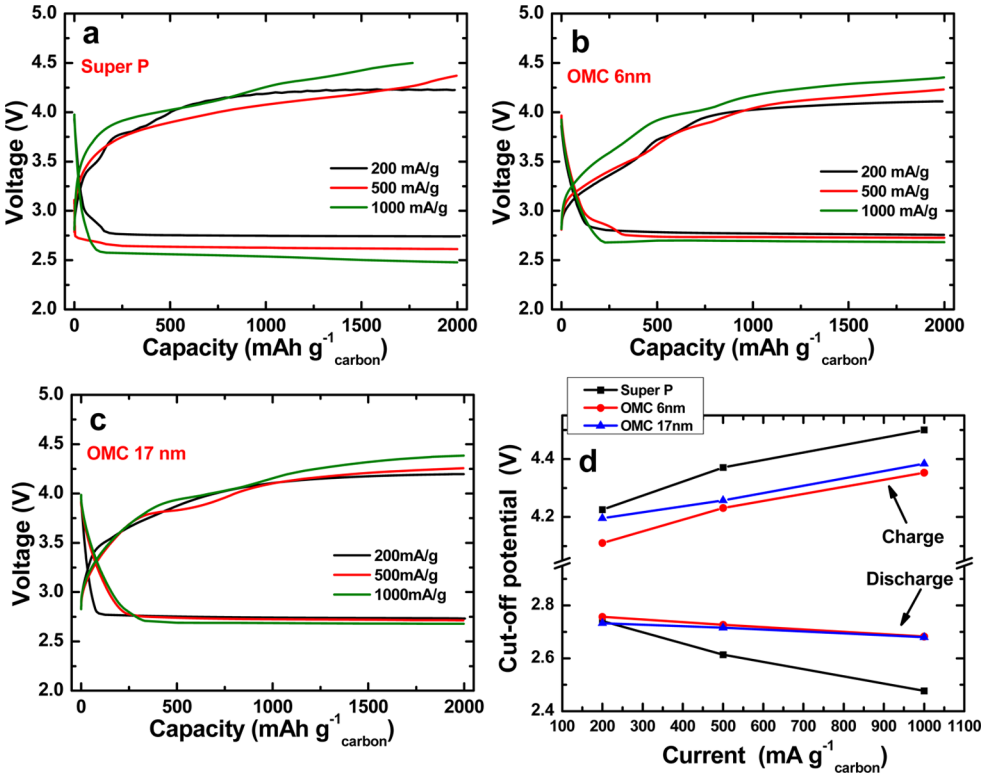

Figure 6. Voltage profile of the charge–discharge test in different current density of 200 mA g^{-1}_{carbon}, 500 mA g^{-1}_{carbon}, and 1000 mA g^{-1}_{carbon} using a (a) super P electrode, (b) OMC-6 electrode, and (c) OMC-17 electrode. (d) Cell voltage vs current density. Capacity was limited to 2000 mAh g^{-1}_{carbon}.

case, the pores of OMC limited the size of Li_2O_2 and crystallinity.

The XRD and TEM results suggest that the contact area between the electrode and Li_2O_2 will affect the electronic conductivity and the rate capability. Figure 6 shows the rate capability of the oxygen electrodes made of OMC-6, OMC-17, and super P carbon. In the super P case shown in Figure 6a, the discharge potential decreased by 0.08 V at higher current conditions. The charge potential at a current of 1000 mA g^{-1}_{carbon} reaches 4.5 V as a cutoff voltage before finishing the charge process. On the other hand, the cathode using OMC-6 and OMC-17 has a lower polarization than super P, as shown in panels b and c in Figure 6. Figure 6d shows that the difference of the cutoff potential in discharge using the super P electrode was five times higher than OMC-17 between the current density of 200 and 1000 mA g^{-1}_{carbon}, as expected, because the former has a well-defined crystallinity and lower electronic conductivity than latter. In the case of OMC-6, its discharge potential was always higher than that of OMC-17, because the OMC-6 electrode has more pores per unit volume and higher exposed surface area. Interestingly, the discharge cutoff potential gap of OMC-6 electrode in a current density between 200 and 1000 mA g^{-1} was greater than OMC-17 by 0.02 V at the same current conditions likely because the oxygen and Li^+ ions more easily penetrated into the larger pores in OMC-17. In the charge process, the charge cutoff potential of OMC-6 electrode, 4.35 V at a current of 1000 mA g^{-1}_{carbon}, was the lowest among the three electrodes as the OMC-6 electrode had a small diameter of lithium peroxide in the pores. On the other hand, the charge cutoff potential gap of the OMC-17 electrode in a current density between 200 mA g^{-1} and 1000 mA g^{-1} is the smallest among the three electrodes because oxygen was also evolved in the charge process and Li^+ ions can more easily escape from the larger pores. Because of the highly developed crystallinity of Li_2O_2 and the extremely small contact area between super P and Li_2O_2, the rate capability of the super P electrode was inferior compared to that of the two OMC electrodes.

CONCLUSIONS

We synthesized ordered mesoporous carbon with two different pore sizes to be used as an oxygen electrode for Li–O_2 cells. From the BET, SAXS, SEM and TEM data, we confirmed that the OMCs had highly ordered mesoporous pores. The XRD and TEM results of the discharged oxygen electrodes demonstrated that the OMC channel limited the Li_2O_2 size. As a result, this process lowers the crystallinity of Li_2O_2 formed in discharging and forces Li_2O_2 to be formed in OMC channels. The oxygen electrode using OMC showed high efficiency and rate capability by changing the structure of the carbon substrate in Li–O_2 cells.

AUTHOR INFORMATION

Corresponding Author

*E-mail: yksun@hanyang.ac.kr

Notes

The authors declare no competing financial interest.

ACKNOWLEDGMENTS

This work was supported by the Human Resources Development of the Korea Institute of Energy Technology Evaluation and Planning (KETEP) grant funded by the Korea government Ministry of Knowledge Economy (20124010203310) and by

the National Research Foundation of Korea (NRF) grant funded by the Korea government (MEST) (2009-0092780).

REFERENCES

(1) Abraham, K. M.; Jiang, Z. *J. Electrochem. Soc.* **1996**, *143*, 1−5.
(2) Bruce, P. G.; Freunberger, S. A.; Hardwick, L. J.; Tarascon, J.-M. *Nat. Mater.* **2012**, *11*, 19−29.
(3) Scrosati, B.; Hassoun, J.; Sun, Y.-K. *Energy Environ. Sci.* **2011**, *4*, 3287−3295.
(4) Freunberger, S. A.; Chen, Y.; Peng, Z.; Griffin, J. M.; Hardwick, L. J.; Barde, F.; Novak, P.; Bruce, P. G. *J. Am. Chem. Soc.* **2011**, *133*, 8040−8047.
(5) Shao, Y.; Ding, F.; Xiao, J.; Zhang, J.; Xu, W.; Park, S.; Zhang, J.-G.; Wang, Y.; Liu, J. *Adv. Funct. Mater.* **2013**, *23*, 987−1004.
(6) Hardwick, L. J.; Bruce, P. G. *Curr. Opin. Solid State Mater. Sci.* **2012**, *16*, 178−185.
(7) Xiao, J.; Mei, D.; Li, X.; Xu, W.; Wang, D.; Graff, G. L.; Bennett, W. D.; Nie, Z.; Saraf, L. V.; Aksay, I. A.; Liu, J.; Zhang, J.-G. *Nano Lett.* **2011**, *11*, 5071−5078.
(8) Mitchell, R. R.; Gallant, B. M.; Thompson, C. V.; Shao-Horn, Y. *Energy Environ. Sci.* **2011**, *4*, 2952−2958.
(9) Yang, Y.; Shi, M.; Zhou, Q.-F.; Li, Y.-S.; Fu, Z.-W. *Electrochem. Commun.* **2012**, *20*, 11−14.
(10) Harding, J. R.; Lu, Y.-C.; Tsukada, Y.; Shao-Horn, Y. *Phys. Chem. Chem. Phys.* **2012**, *14*, 10540−10546.
(11) Lu, Y.-C.; Xu, Z.; Gasteiger, H. A.; Chen, S.; Hamad-Schifferli, K.; Shao-Horn, Y. *J. Am. Chem. Soc.* **2010**, *132*, 12170−12171.
(12) Debart, A.; Paterson, A. J.; Bao, J.; Bruce, P. G. *Angew. Chem., Int. Ed.* **2008**, *47*, 4521−4524.
(13) Xu, J.-J.; Xu, D.; Wang, Z.-L.; Wang, H.-G.; Zhang, L.-L.; Zhang, X.-B. *Angew. Chem., Int. Ed.* **2013**, *52*, 3887−3890.
(14) Wang, L.; Zhao, X.; Lu, Y.; Xu, M.; Zhang, D.; Ruoff, R. S.; Stevenson, K. J.; Goodenough, J. B. *J. Electrochem. Soc.* **2011**, *158*, A1379−A1382.
(15) Jung, H.-G.; Jeong, Y. S.; Park, J.-B.; Sun, Y.-K.; Scrosati, B.; Lee, Y. J. *ACS Nano* **2013**, *7*, 3532−3539.
(16) San, C. H.; Hong, C. W. *J. Electrochem. Soc.* **2012**, *159*, K116−K121.
(17) Sun, B.; Wang, B.; Su, D.; Xiao, L.; Ahn, H.; Wang, G. *Carbon* **2012**, *50*, 727−733.
(18) Guo, Z.; Zhou, D.; Dong, X. L.; Qiu, Z.; Wang, Y.; Xia, Y. *Adv. Mater.* **2013**, *25*, 5668−5672.
(19) Xu, J.-J.; Wang, Z.-L.; Xu, D.; Zhang, L.-L.; Zhang, X.-B. *Nat. Commun.* **2013**, *4*, 2438.
(20) Ying, J. Y.; Mehnert, C. P.; Wong, M. S. *Angew. Chem., Int. Ed.* **1999**, *38*, 56−77.
(21) Kresge, C. T.; Leonowicz, M. E.; Roth, W. J.; Vartuli, J. C.; Beck, J. S. *Nature* **1992**, *359*, 710−712.
(22) Shitta-Bey, G. O.; Mirzaeian, M.; Hall, P. J. *J. Electrochem. Soc.* **2012**, *159*, A315−A320.
(23) Wang, Z.-L.; Xu, D.; Xu, J.-J.; Zhang, L.-L.; Zhang, X.-B. *Adv. Funct. Mater.* **2012**, *22*, 3699−3705.
(24) Liu, R.; Shi, Y.; Wan, Y.; Meng, Y.; Zhang, F.; Gu, D.; Chen, Z.; Tu, B.; Zhao, D. *J. Am. Chem. Soc.* **2006**, *128*, 11652−11662.
(25) Hwang, J.; Woo, S. H.; Shim, J.; Jo, C.; Lee, K. T.; Lee, J. *ACS Nano* **2013**, *7*, 1036−1044.
(26) Shim, J.; Lee, J.; Ye, Y.; Hwang, J.; Kim, S.-K.; Lim, T.-H.; Wiesner, U.; Lee, J. *ACS Nano* **2012**, *6*, 6870−6881.
(27) Tanev, P.; Pinnavaia, T. *Science* **1995**, *267*, 865−867.
(28) Simon, P. F.; W. Ulrich, R.; Spiess, H. W.; Wiesner, U. *Chem. Mater.* **2001**, *13*, 3464−3486.
(29) Abraham, K. M.; Jiang, Z.; Carroll, B. *Chem. Mater.* **1997**, *9*, 1978−1988.
(30) Laoire, C. Ó; Mukerjee, S.; Plichta, E. J.; Hendrickson, M. A.; Abraham, K. M. *J. Electrochem. Soc.* **2011**, *158*, A302−A308.
(31) Jung, H.-G.; Kim, H.-S.; Park, J.-B.; Oh, I.-H.; Hassoun, J.; Yoon, C. S.; Scrosati, B.; Sun, Y.-K. *Nano Lett.* **2012**, *12*, 4333−4335.
(32) Adams, B. D.; Radtke, C.; Black, R.; Trudeau, M. L.; Zaghib, K.; Nazar, L. F. *Energy Environ. Sci.* **2013**, *6*, 1772−1778.